CHAPTER- 5

MnO_x /CeO_2 Catalysts for the Low-Temperature Selective Catalytic Reduction of NO with NH_3

Abstract

The development of efficient MnO_x based catalysts has received wide application due to its variable oxidation state and crystal structure. Furthermore, catalytic activity of MnO_x supported on various transition metal oxides (TiO_2, ZrO_2, CeO_2, Al_2O_3) has shown high performance for low temperature SCR catalysts. [1,2]

Since, morphology of ceria can influence the catalytic activity as they expose different crystal planes and atomic arrangements, therefore, in this work, ceria nanorods were used as catalyst support and MnO_2, Mn_2O_3, and MnO oxides were impregnated on the support in anticipation of increasing the performance of NH_3-SCR reaction for NO removal.

5.1. Experimental

5.1.1. Materials and methods

The chemical and gases used in the experiments were purchased commercially and were used without further treatment. The chemical and reagents used were cerium (III) nitrate hexahydrate ($Ce(NO_3)_3 \cdot 6H_2O$, 99.0% purity, SRL Pvt. Ltd), sodium hydroxide (NaOH, 98% purity Chemika- biochemika-reagents), ethanol (99% purity, SD fine-chemical limited), Manganese nitrate tetra-hydrate ($MnN_2O_6.4H_2O$, ≥ 97% purity, SRL Pvt. Ltd), Manganese (II) oxide (MnO, 99% purity, Sigma-Aldrich), Manganese (III) oxide (MnO, 99% purity, Sigma-Aldrich) and Manganese (IV) oxide (MnO_2, 98% purity, alfa aesar). Deionized water was used for the preparation of aqueous solutions. The gases used were NH_3 (1000 ppm, Ar balanced),

NO (1000 ppm, Ar balanced), O_2 (6 vol %, Ar balanced), and N_2 (99.999%) in the activity valuation experiments.

5.1.2. Catalysis synthesis

5.1.2.1. Support synthesis

The hydrothermal method was used to synthesize ceria nanorod supports; for this 5 mmol of an aqueous cerium nitrate hexahydrate was mixed with of NaOH (7 mmol) solution, and the mixed solution was further mixed continuously for 1 h. The obtained homogenous solution was put into a 100 mL Teflon-lined autoclave to carry out the hydrothermal process at the reaction temperature of 100℃ for 5 h. Further, to remove any possible ionic impurities, the precipitate was first cooled to room temperature and then washed 3-4 times with de-ionized water and ethanol. Then, the precipitate was put in the oven for 12 h at 80℃, and the obtained sample was calcined at 500℃ for 5 h and labelled as CeO_2-NR (nanorod) in the manuscript.

5.1.2.2. Catalyst synthesis

Metal oxides of MnO_2, MnO, and Mn_2O_3 were impregnated on the CeO_2-NR using the wet-impregnation method. The calculated amount (5wt.%) of commercial MnO_2, MnO, and Mn_2O_3 were mixed into an aqueous solution of CeO_2-NR, and mixtures were stirred till the metal oxide and support gets homogeneously mixed, and then homogenous solution was put in air-oven for drying at 100℃ overnight followed by calcination at 500℃ for 4 h. These synthesized catalysts are denoted as MnO_2/CeO_2-NR, MnO/CeO_2-NR, and Mn_2O_3/CeO_2-NR in the manuscript.

5.2. Results and discussion

5.2.1. Brunauer–Emmett–Teller (BET)

The results of Ceria supports' and catalysts' N_2 adsorption-desorption isotherms are shown in **Fig. 5.1**. All these isotherm curves fit into the type IV group, confirming that the synthesized catalysts were mesoporous materials. [3] The surface area, pore volume, and average pore size

of the catalysts were evaluated using N_2 adsorption-desorption and are summarized in **Table 5.1**. **Table 5.1** shows the reduced surface area, pore volume, and pore diameter after the impregnation of active metals (MnO, MnO_2, Mn_2O_3). The MnO_2/CeO_2-NR catalyst showed the highest BET surface area (12.04 $m^2.g^{-1}$) compared to MnO/CeO_2-NR (7.46 $m^2.g^{-1}$) and Mn_2O_3/CeO_2-NR (10.76 $m^2.g^{-1}$). The catalysts decreased BET surface area and pore volume because MnO_x blocked the pores of the CeO_2-NR during the catalyst synthesis process. However, the MnO_2/CeO_2-NR catalysts' BET surface area and pore volume are higher than those of the other catalysts after the impregnation of MnO_2 because some MnO_2 has dispersed on the surface of the CeO_2-NR support, while some have blocked pores. The average particle size of MnO_2/CeO_2-NR catalysts is also smaller compared to the other two catalysts, which also supports a high surface area compared to the other catalysts. [4,5]

Table 5.1. Physicochemical properties, crystal size and average particles size of catalysts

Catalysts	**Surface area S_{BET} ($m^2.g^{-1}$)**	**Pore volume V_p ($cm^3.g^{-1}$)**	**Average pore size (nm)**
CeO_2 - NR	17.63	0.124	8.71
MnO_2/CeO_2 - NR	12.04	0.105	8.76
Mn_2O_3/CeO_2 - NR	10.77	0.076	8.70
MnO/CeO_2 - NR	7.46	0.015	7.94

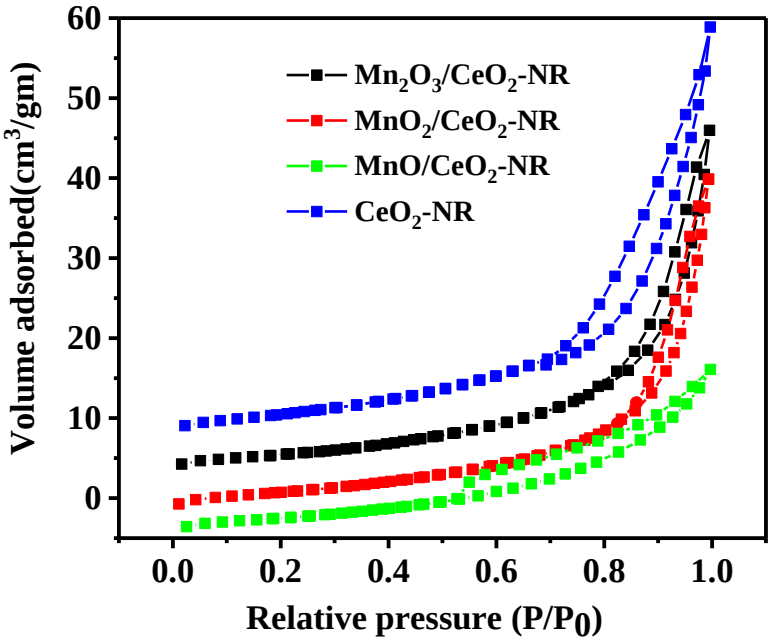

Fig. 5.1. N_2 adsorption and desorption isotherms of supports and catalysts

5.2.2. X-Ray Diffraction *(*XRD)

For the crystal structures and phase identification, the prepared samples were characterized via XRD. **Fig.5.2** shows the obtained XRD pattern of the characterized samples. The patterns showed the intensive diffraction peaks for all the three catalysts and CeO_2-NR supports, at $2\theta = 28.4$, 33.2, 47.4, 56.4, 59.2, 69.4, 76.5, and 79.2, can be ascribed to the (1 1 1), (2 0 0), (2 2 0), (3 1 1), (2 2 2), (4 0 0), (3 3 1), and (4 2 0) plane diffraction of the cubic face-centered structure of CeO_2 (JCPDS card, No. 81, 0792, a=b=c=5.412 Å), tetragonal pirimitive (JCPDS card, No. 81,2261, a=b=4.404 Å, c=2.876 Å) for MnO_2, cubic face-centered (JCPDS card, No. 89, 4835, a=b=c=4.443 Å) for MnO and cubic body-centered (JCPDS card, No. 89, 2809, a=b=c=9.420 Å) for Mn_2O_3**.** The average crystal size of the catalysts slightly increased after impregnation of active metals, shown in the **Table 5.2**. The diffraction peaks of manganese were not detected in any catalysts after impregnation of different manganese oxides on the CeO_2-NR, suggesting that all these active metals were well dispersed on the surface of the CeO_2-NR [6,7].

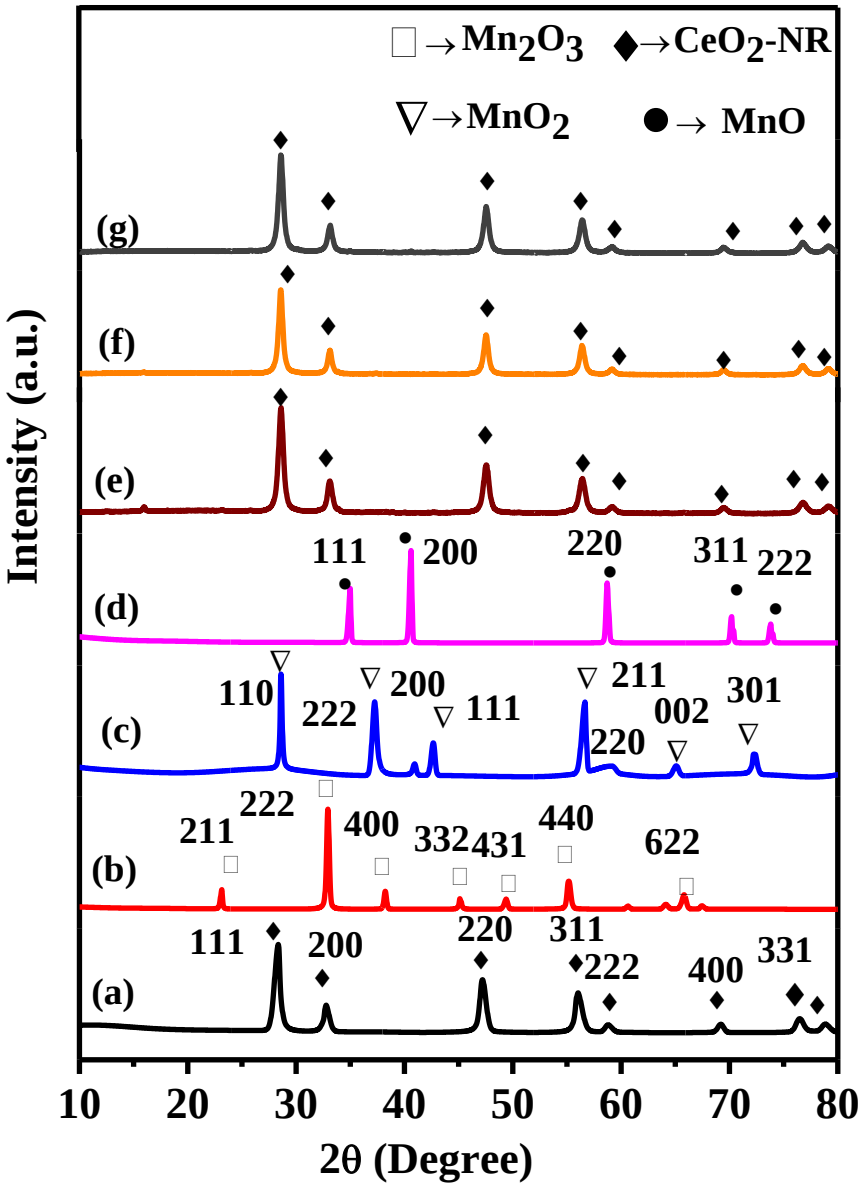

Fig. 5.2. XRD patterns of (a) CeO_2-NR, (b) Mn_2O_3, (c) MnO_2, (d) MnO, (e) Mn_2O_3/CeO_2-NR, (f) MnO_2/CeO_2-NR and (g) MnO/CeO_2-NR

Table 5.2. The average crystal size, lattice parameters, and particle size of the samples

Catalysts	Average crystal size (nm)[a]	Average particles size (nm)[b]	Lattice parameter (Å)	Lattice strain ((Δd/d) [c]
CeO_2 - NR	12.52	45.85	5.412	0.0178
MnO_2/CeO_2 - NR	12.94	61.68	5.416	0.0293
Mn_2O_3/CeO_2 - NR	14.21	81.39	5.414	0.0286
MnO/CeO_2 - NR	13.30	89.50	5.410	0.0211

[a] *Scherrer equation*, [b] *Particle size calculated from TEM image data*, [c] *Williamson-Hall method.*

5.2.3. X-ray Photoelectron Spectroscopy (XPS)

XPS analysis was performed to investigate the surface chemical properties of all catalysts in terms of oxidation states and species of surface atoms. The XPS spectra of Ce 3d, Mn 2p and O 1s are shown in **Fig. 5.3**, and **Fig. 5.4**.

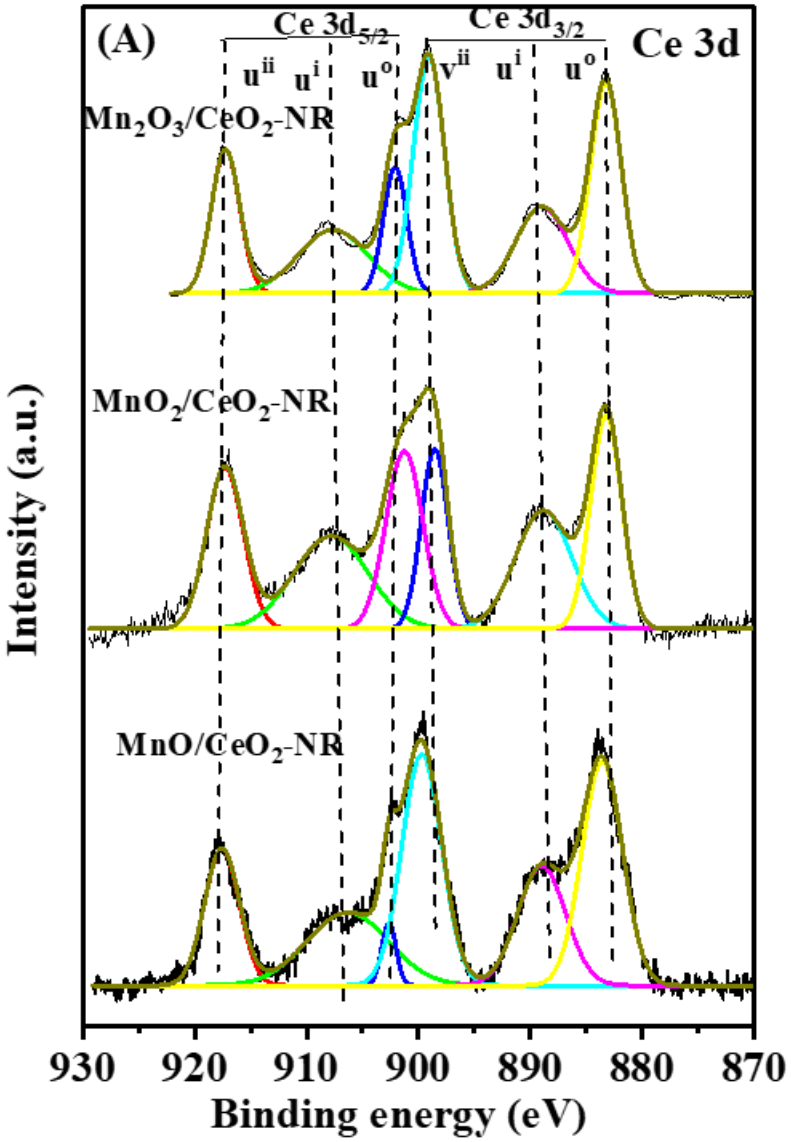

Fig. 5.3. XPS spectra of Ce 3d of catalysts

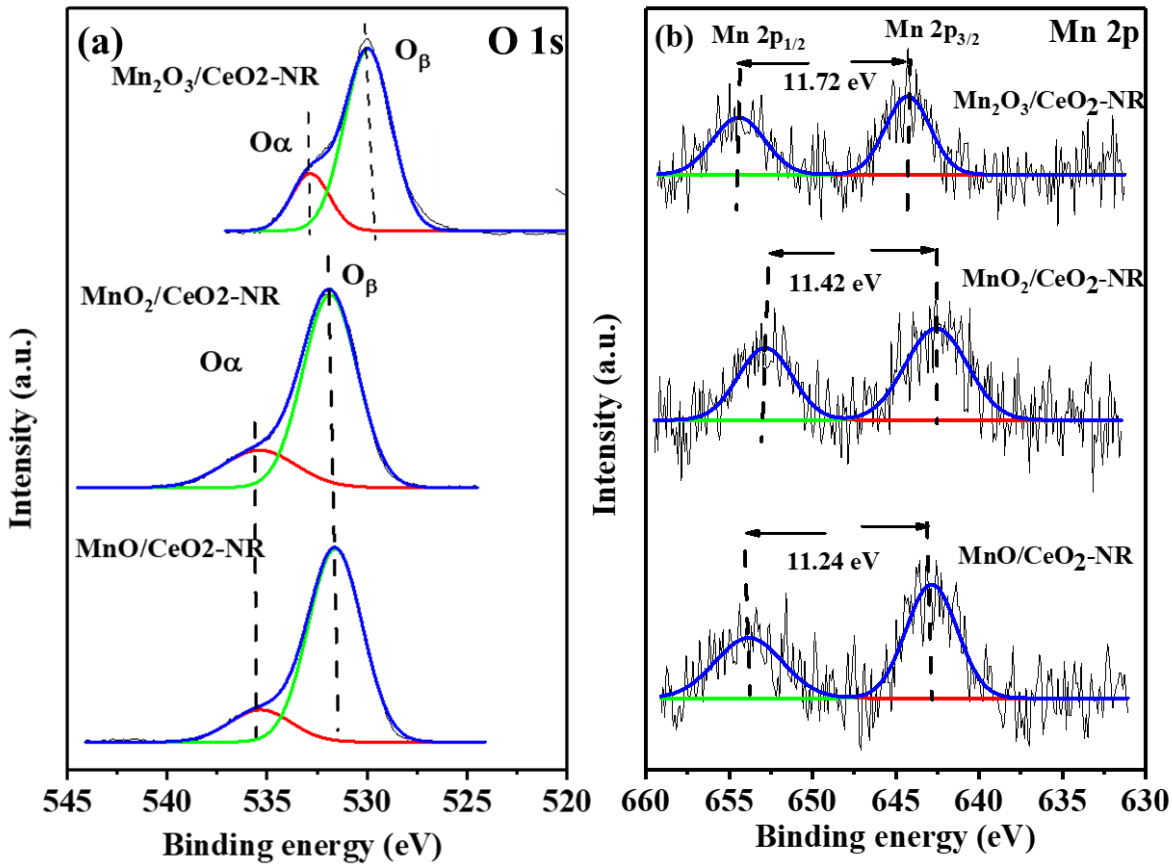

Fig. 5.4. XPS spectra of (a) O 1s and (b) Mn 2p of the catalysts

Table 5.3. XPS result of Mn 2p for the MnO/CeO_2-NR, MnO_2/CeO_2-NR and Mn_2O_3/CeO_2-NR

Catalysts	Mn^{4+} Be (eV)	Mn^{3+} Be (eV)	(Mn^{4+}/ Mn^{4+}+Mn^{3+}) %
Mn_2O_3/CeO_2-NR	644.13	654.36	64.0
MnO/CeO_2-NR	642.63	653.06	62.0
MnO_2/CeO_2-NR	642.93	653.96	68.0

Table 5.4. XPS results of Ce 3d and O 1s for the MnO/CeO_2-NR, MnO_2/CeO_2-NR and Mn_2O_3/CeO_2-NR

Catalysts	O_α Be (eV)	O_β Be (eV)	$(O_\alpha/ O_\alpha+O_\beta)$ %	$(Ce^{3+}/Ce^{3+}+Ce^{4+})$ %
Mn_2O_3/CeO_2-NR	532.71	530.06	29.1	38.8
MnO/CeO_2-NR	535.60	531.86	27.2	37.4
MnO_2/CeO_2-NR	535.54	531.69	31.5	39.8

The Ce 3d spectra of CeO_2 support and catalysts are shown in **Fig.5.3**. The spectra are classified as two sets of spin orbital lines, which are marked as u and v corresponding to $3d_{3/2}$ and $3d_{5/2}$, respectively. In **Fig.5.3,** the u°, u^{I}, u^{II}, v°, v^{I}, and v^{II} were used to represent the Ce 3d spectra of the studied catalysts. The spin-orbit doublet peak series shown by u and v, respectively, reflect the Ce $3d_{3/2}$ and Ce $3d_{5/2}$ states. [8] The synthesized catalysts, which have cerium oxide, contain both the tri-valent and the tetra-valent cerium ions. The labels of only two peaks, u° (899.50 eV) and v° (917.50 eV), are ascribed to Ce^{3+} ions species, whereas u^{I} (889.55 eV), u^{II} (883.74 eV), v^{I} (908.76 eV), and v^{II} (899.54 eV) are given to Ce^{4+} ions species. The de-convoluted split peaks confirm the existence of Ce^{3+} and Ce^{4+} ions in cerium di-oxides. The proportion of lattice oxygen amount and the surface amount ion content of Ce^{3+} had a significant effect on the materials' performance. Due to a higher quantity of oxygen vacancy at the CeO_2 and MnO_2 interface, the Ce^{3+} concentration of the MnO_2/CeO_2-NR catalyst is 39.81%, which is higher among all the catalysts, as shown in **Table 5.4**.

Fig. 5.4(a) shows the corresponding O1s XPS patterns for the catalysts; the deconvoluted O 1 s spectra clearly show two surface oxygen species, denoted as O_β and O_α, respectively. The peak at around 528.9–532.1 eV can be assigned to lattice oxygen (O_β) and peak at around 533.3–535.7 eV can be attributed to chemisorbed oxygen species (O_α). The ratio of O_α/

($O_\alpha + O_\beta$) was calculated to evaluate the concentration of oxygen vacancies (**Table 5.4**). The results showed that atomic ratio of O_α for the MnO_2/CeO_2-NR (31.5%) catalyst is higher than the MnO/CeO_2-NR (27.20%) and Mn_2O_3/CeO_2-NR (29.1%) catalysts. The NH_3-SCR reaction benefits from a higher $O_\alpha/(O_\alpha + O_\beta)$ relative concentration ratio, which promotes the oxidation of NO to NO_2 and thus facilitates the 'fast SCR' process.[9]

The XPS pattern of Mn2p for the MnO_2/CeO_2-NR, MnO/CeO_2-NR, and Mn_2O_3/CeO_2-NR catalysts are shown in **Fig. 5.4.(b)** High-resolution Mn2p XPS spectra reveal the binding energy doublets at 654.86 eV ($Mn2p_{3/2}$) and 643.14 eV ($Mn2p_{1/2}$), which indicates the Mn^{4+} and Mn^{3+}, respectively [10,11]. It is noted that the spin-orbit splitting value predicted for the doublet Mn2p is 11.72 eV, which is almost the same as the value published for Mn_2O_3 [12,13]. Mn^{4+} and Mn^{3+} were regarded as the primary valence states influencing the catalysts' redox characteristics. The MnO_2/CeO_2-NR spectrum of MnO_2 is shown in the middle graph of **Fig. 5.4(b)**. The two peaks at 642.63 and 653.21 eV with an energy separation of 11.42 eV in the Mn2p spectrum of MnO_2 can be attributed to $Mn2p_{3/2}$ and $Mn2p_{1/2}$. These results show that the oxidation state of Mn is +4, which is consistent with the published MnO_2 values [14,15]. For the MnO/CeO_2-NR catalyst, the bottom graph in **Fig. 5.4(b)**, the separation between the 654.66 eV ($Mn2p_{3/2}$) and 643.42 eV ($Mn2p_{1/2}$) was found to be 11.24 eV, which agrees with the characteristics of MnO [16,9]. Both Mn^{4+} and Mn^{3+} were regarded to be the primary valence states that influenced the catalysts redox characteristics. Also, Mn^{4+} was a key component, and a high Mn^{4+} concentration could speed up the SCR reaction by promoting the conversion of NO to NO_2. Among all, the MnO_2/CeO_2-NR catalyst has the highest ratio of $Mn^{4+}/(Mn^{3+}+Mn^{4+})$ (68%) and the results are shown in **Table 5.3**.

5.2.4. Transmission Electron Microscopy (TEM)

The images of supports and catalyst from TEM, selected area electron diffraction (SAED), and histograms are exhibited in **Fig.5.5**. **Fig.5.5(a)** shows the TEM image of the CeO_2-NR, while **Fig.5.5(b)**, **Fig.5.5(c)** and **Fig.5.5(d)** shows the TEM images of MnO_2/CeO_2-NR, Mn_2O_3/CeO_2-NR and MnO/CeO_2-NR catalysts respectively. TEM images of the catalysts showed that the morphology of the supports is not affected after the impregnation of active metals. Further, the obtained SAED patterns confirm that the samples prepared are crystalline in nature, in line with the XRD results, already described in XRD section. Histograms disclose that the average particle size of all the catalysts was increased after impregnation of active metals, and average particles size is 45.85, 61.68, 81.39 and 89.50 nm for CeO_2-NR, MnO_2/CeO_2-NR, Mn_2O_3/CeO_2-NR and MnO/CeO_2–NR catalysts respectively as shown in **Table 5.2**.

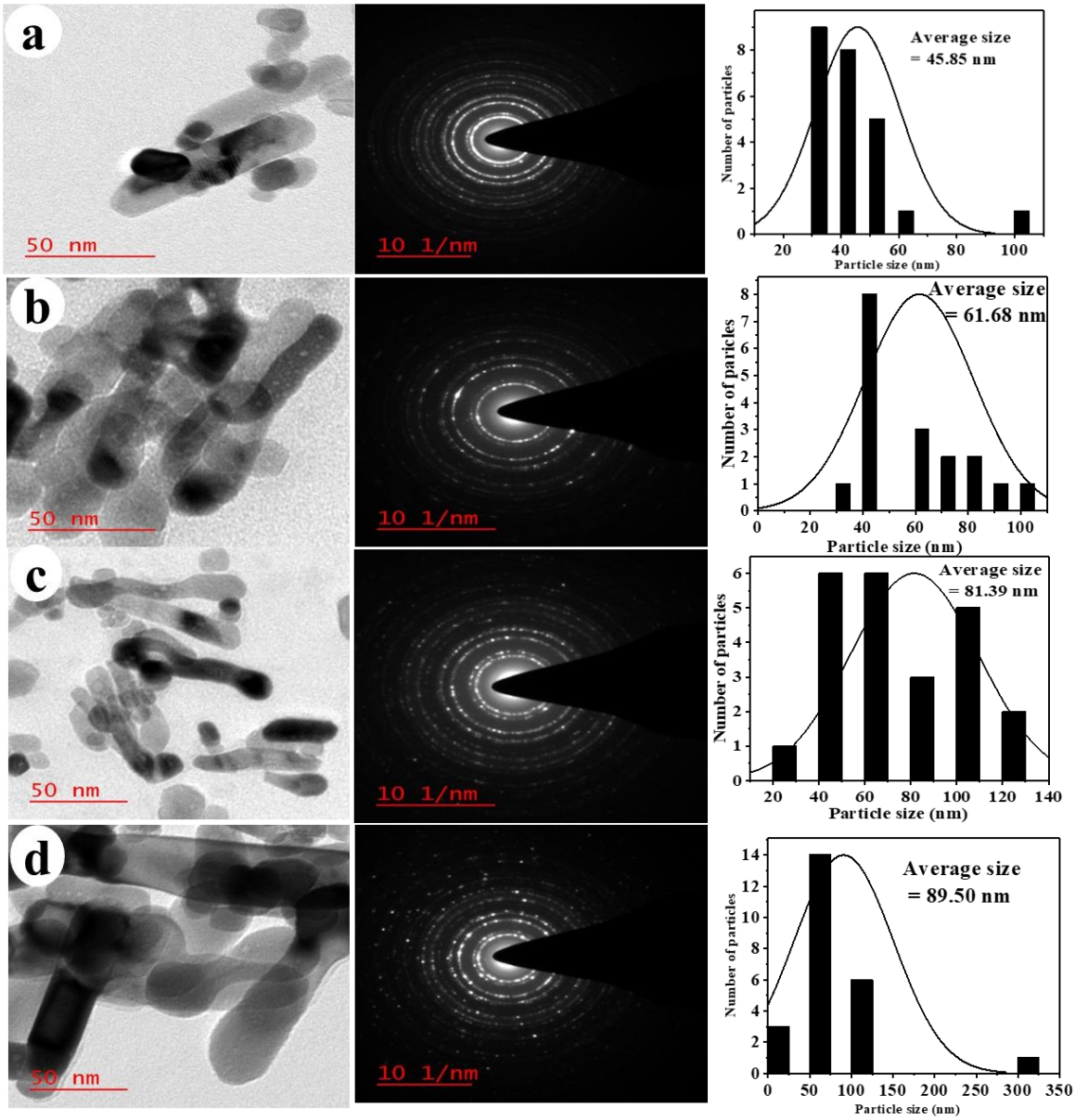

Fig. 5.5. TEM images of (a) CeO_2-NR, (b) MnO_2/CeO_2-NR, (c) Mn_2O_3/CeO_2-NR, and (d) MnO/CeO_2-NR

5.2.5. Scanning Electron Microscopy-Energy Dispersive X-ray Spectroscopy (SEM-EDX)

For the extra surface information of the catalysts, the SEM-EDX and elemental mapping study was done, which are shown in the **Fig.5.6** and **Fig. 5.7** respectively. **Fig. 5.6(a)** shows the SEM-EDX images of the CeO_2-NR supports, while **Fig. 5.6(b)**, **Fig. 5.6(c)**, and **Fig. 5.6(d)** show the

results for the Mn_2O_3/CeO_2-NR, MnO_2/CeO_2-NR, and MnO/CeO_2-NR, respectively. It is also observed that on the supports before the active metal impregnation, the surface is smooth (**Fig.5.6(a)**), but after impregnation, the roughness increases (**Fig.5.6(b)**, **Fig.5.6(c)**, and **Fig. 5.6(d)**). It means that a rougher surface will provide more reaction sites.

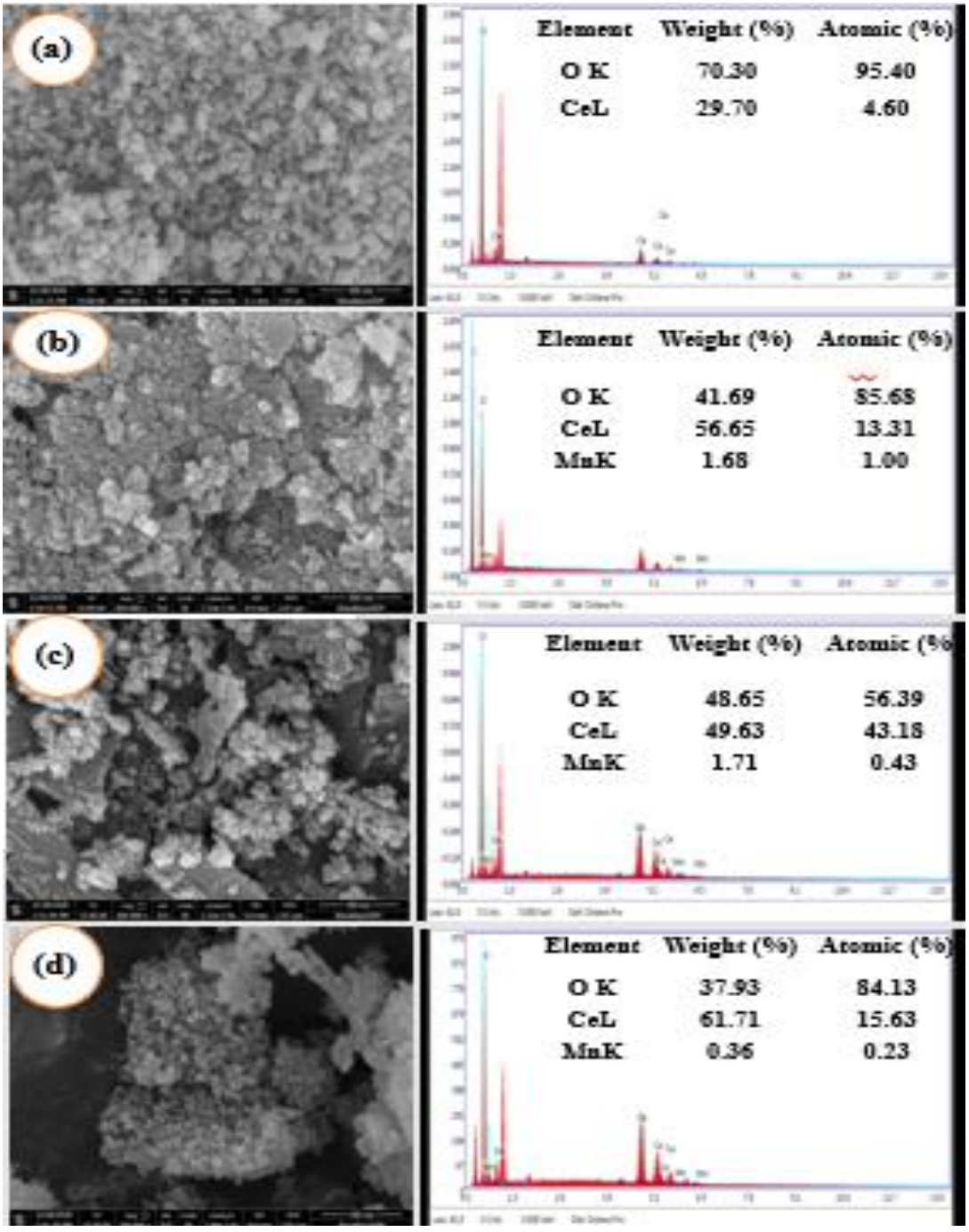

Fig. 5.6. SEM-EDX images of CeO_2 support and catalysts

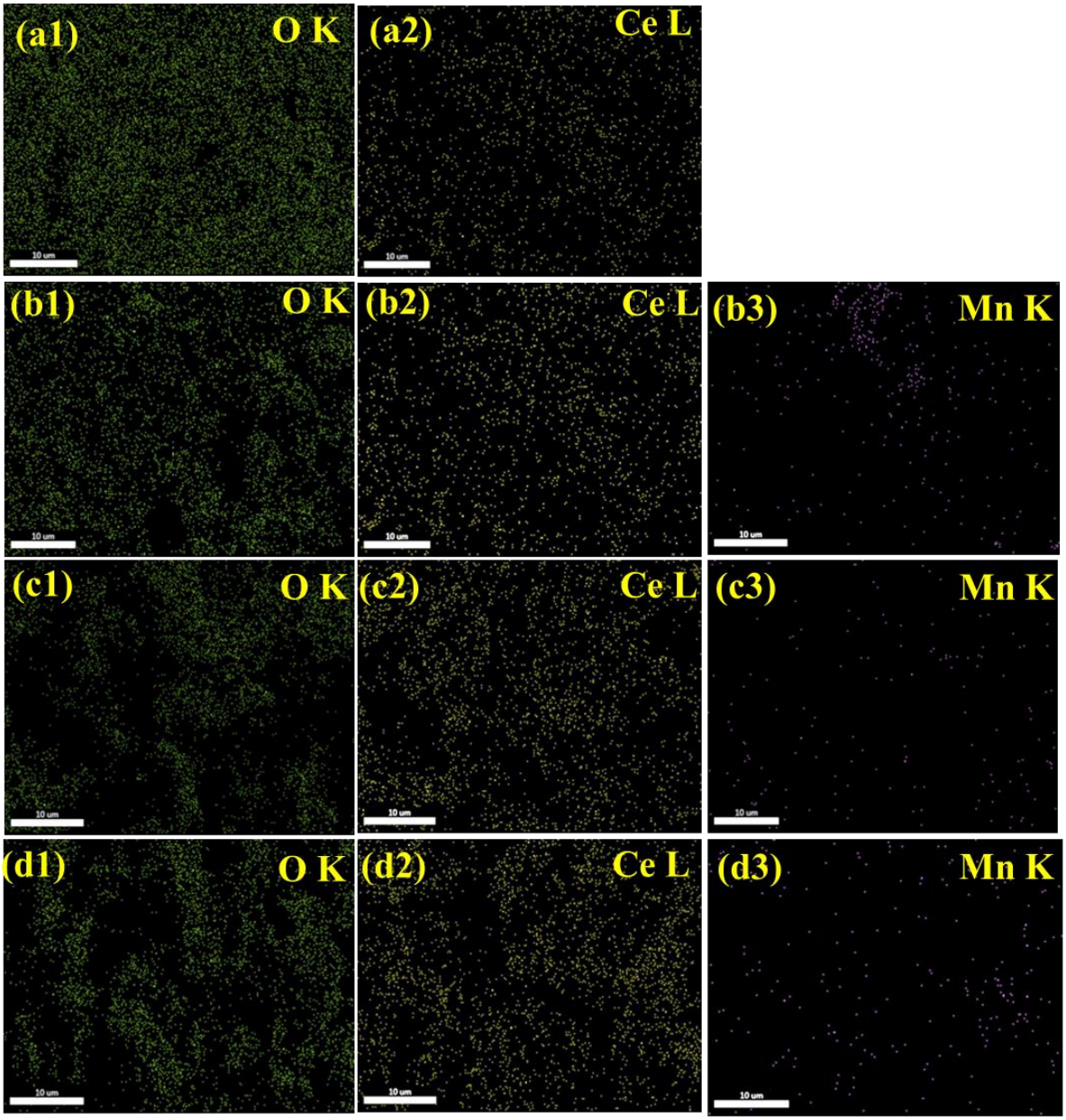

Fig. 5.7. Elemental mapping of CeO_2 (a1, a2), MnO_2/CeO_2(b1, b2, b3), MnO/CeO_2 (c1, c2, c3), Mn_2O_3/CeO_2(d1, d2, d3)

The composition analysis of samples was done through the EDX and elemental mapping. The EDX and elemental mapping results (**Fig.5.7**) confirmed that the active MnO_x is present in the catalysts, which indicated that the active metal is successfully impregnated in the catalysts. The EDX spectra of the catalysts (**Fig.5.6(b)**, **Fig.5.6(c)**, and **Fig.5.6(d)**) show that all the elements O, Ce, and Mn are present, and there is no extra residue present in the sample. As shown in

Fig.5.7, the percentage and distribution of Mn and O were higher and more homogenous in catalysts (**Fig.5.6(c)**) than in the other two catalysts (**Fig.5.6(b)** and **Fig.5.6(d)**).

5.2.6. Hydrogen-Temperature Programmed Reduction (H_2-TPR)

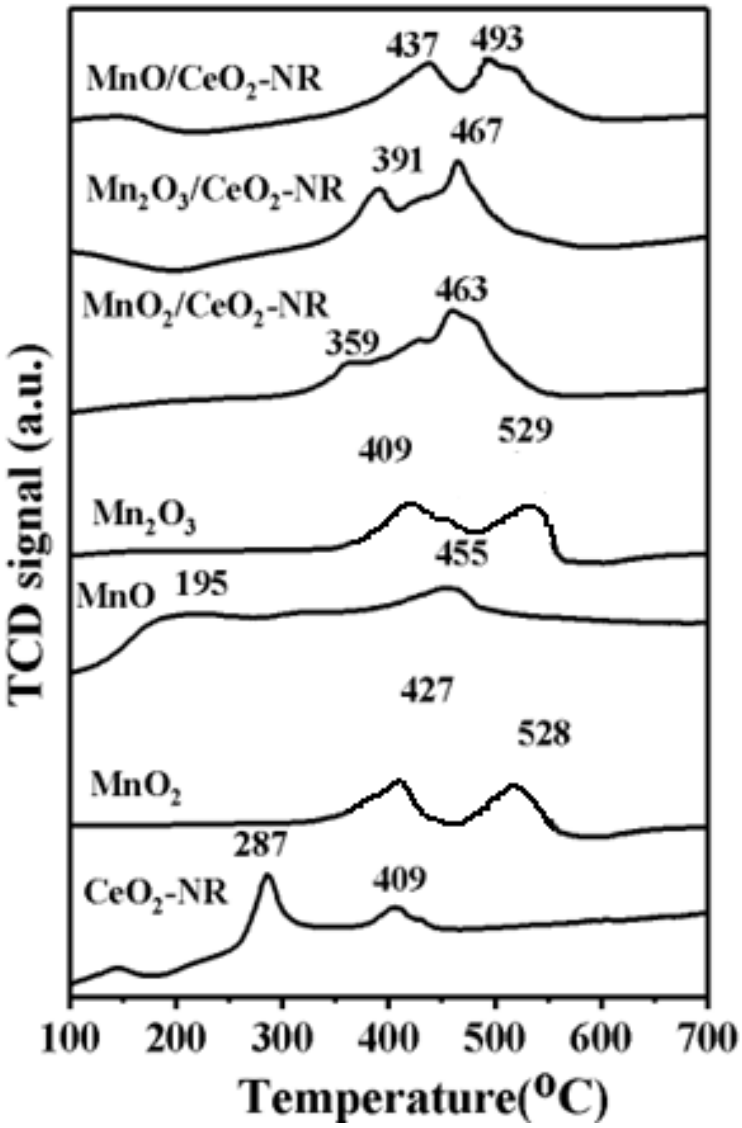

Fig. 5.8. H_2-TPR of MnO_2, MnO, Mn_2O_3, CeO_2-NR and catalysts

H_2-TPR analysis was performed to study the metal support interaction and reducibility of catalysts and the results are shown in **Fig. 5.8.** The TPR profile of CeO_2-NR exhibited two reduction peaks at 287°C and 409°C which attributes to reduction of surface oxygen. Two

major reduction peaks were observed for all the MnO_x species in the range of 150-550 ° C. According to the literature, these peaks can be recognized to sequential reduction of MnO_x species i.e $Mn^{4+} \rightarrow Mn^{3+} \rightarrow Mn^{2+}$ (MnO_2 to Mn_2O_3 and Mn_2O_3 to MnO).[17] The peak in lower temperature range can be attributed to Mn^{4+} to Mn^{3+} whereas peak in the higher range can be attributed to reduction of Mn^{3+} to Mn^{2+}. The H_2-TPR analysis of the catalysts showed that, CeO_2-NR peaks migrated towards the high temperature, which may be due to the reduction of Ce^{4+} to Ce^{3+}, implying a significant interaction between manganese and the CeO_2-NR phases. [17,18] **Table 5.5** shows the amount of hydrogen consumed by the support, pure MnO_x species and catalysts in the H_2-TPR experiments. In all these data, the MnO/CeO_2-NR showing the lowest hydrogen consumption while the MnO_2/CeO_2-NR shows the highest.

Table 5.5. H_2-TPR data of catalysts

Sample	Reduction temperature (°C)		Hydrogen consumption ($mmol.gm^{-1}$)
	Lower	Higher	
CeO_2-NR	287	409	1.30
MnO_2	427	528	1.15
MnO	195	455	0.81
Mn_2O_3	409	529	1.33
MnO_2/CeO_2-NR	359	463	2.01
MnO/CeO_2-NR	437	493	1.73
Mn_2O_3/CeO_2-NR	391	467	1.81

5.2.7. Raman Spectroscopy

The lattice vibration and oxygen vacancies of CeO_2 support and catalysts were anaylzed by Raman spectroscopy and the results are shown in **Fig.5.9**. The CeO_2-NR and MnO_x/CeO_2-NR catalysts exhibit a strong band at 475-485 cm^{-1}, corresponding to F_{2g} Raman vibration mode in fluorite structure of CeO_2. In addition, vibration peak around 600 cm^{-1} correspond to oxygen

defect induced (D) mode due to presence of structural defects. As compared with pure CeO_2, the peak intensity shifted slightly to the right when MnO, MnO_2, and Mn_2O_3 were loaded on CeO_2-NR support. The catalyst peak shift indicates strong synergetic effects between Ce and Mn in the crystal lattice. [19,20]

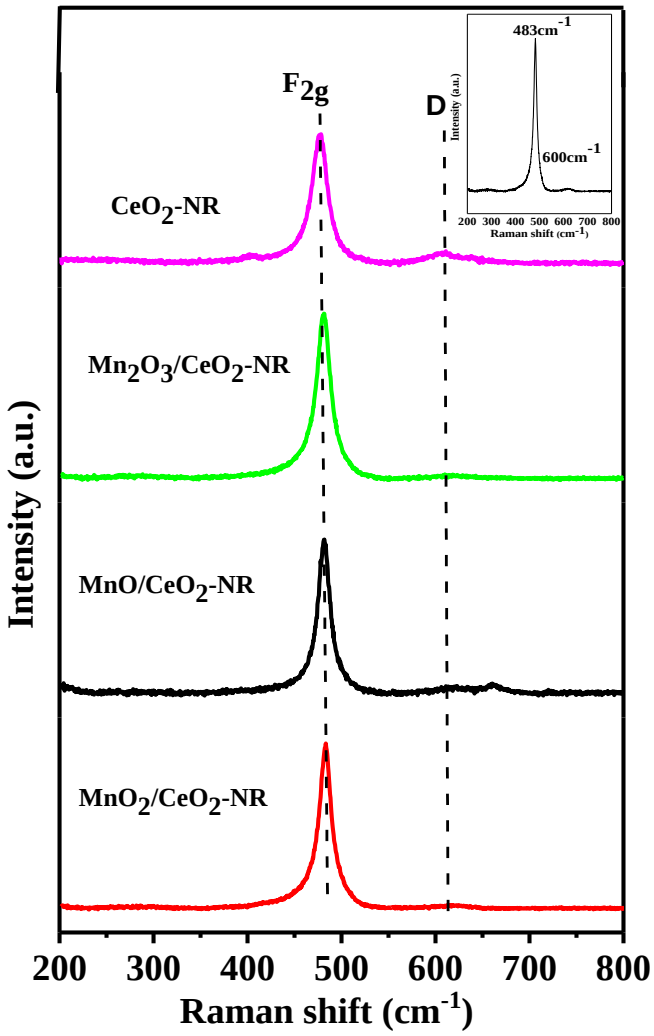

Fig. 5.9. Raman spectra of support and catalysts

According to the literature, the ratio of the peak regions of D-mode to F_2g shows the relative content of oxygen vacancies Accordingly, a higher D/F_2g ratio indicates a higher concentration of oxygen vacancies. [21,22] As shown in the **Fig.5.10**, MnO_x supported catalysts significantly increases the concentration of oxygen vacancy compared to CeO_2 support. The amount of

oxygen concentration is in the order: MnO_2/CeO_2-NR (0.137) > Mn_2O_3/CeO_2-NR (0.068)> MnO/CeO_2-NR (0.037) > CeO_2-NR (0.034). The MnO_2/CeO_2-NR catalyst showed significantly higher oxygen concentration in comparison to other catalysts. The XPS data also confirmed that the oxygen concentration of MnO_2/CeO_2-NR catalyst is highest compared to other catalysts.

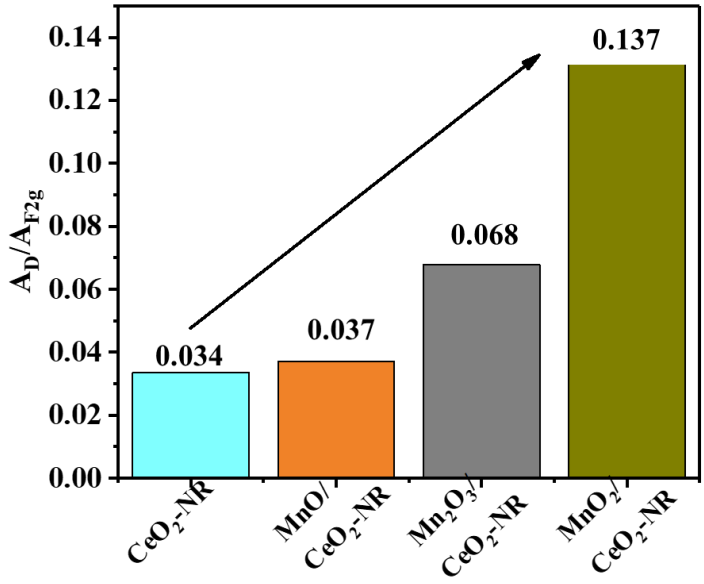

Fig. 5.10. Ratio of A_D/A_{F2g} for CeO_2 support and catalysts

5.2.8. Activity Measurements

5.2.8.1. Effect of temperature on catalyst for NO reduction

The NH_3-SCR activities of the MnO/CeO_2-NR, MnO_2/CeO_2-NR, and Mn_2O_3/CeO_2-NR catalysts in the temperature range 50-450℃ are shown in **Fig. 5.11**. All three catalysts worked in a wide temperature range, and the NO conversion initially increased and gave maximum conversion at 350℃ and then started to decline when the temperature increased. In the graph, the NO conversion rates of the three catalysts were MnO_2/CeO_2-NR > Mn_2O_3/CeO_2-NR > MnO/CeO_2-NR over the given temperature range. The NO conversion of the MnO_2/CeO_2-NR showed the highest, as can be seen in **Fig. 5.11(a)**; when the temperature reached 340℃, 65%

NO conversion and greater than 85% N_2 selectivity were achieved (shown in **Fig. 5.11(b)**). NO conversion is 50.2% and 55.4%, respectively, for the other two catalysts, MnO/CeO_2-NR and Mn_2O_3/CeO_2-NR, while the N_2 selectivity was also between 80 to 87% for both the catalysts. According to the characterization data, the MnO_2/CeO_2-NR has the highest surface area (12.04 $m^2.g^{-1}$) and pore volume (0.105 $cm^3.g^{-1}$) out of three catalysts, as shown in **Table 5.1**, resulting in the most elevated active surfaces and more effective reactant interactions. It also has more surface Ce^{3+} (39.81%) species than the other two catalysts. It also shows a strong interaction between Ce and Mn (as indicated in the Raman characterizations in **Fig. 5.10**) and a greater diversity of surface-active oxygen species (31.5%). From the H_2-TPR also, we can see that after MnO_2 loaded on CeO_2-NR, reduction peaks of MnO_2/CeO_2-NR exhibited broad low-temperature profiles and high-temperature ones, providing the highest performances in a wide range of temperatures, and showing the highest hydrogen consumption. Therefore, the MnO_2/CeO_2-NR catalyst showed better performance.

Equation **(3)** was used to compute the turnover frequency (TOF) for each catalyst at three temperatures: 300, 350, and 400°C, with the results reported in **Table 5.6.** The results showed that temperature, catalyst quantity, and H_2-consumption all affected the TOF. Among all catalysts, MnO/CeO_2-NR had the lowest TOF (1.195 s^{-1}) at 350°C. The TOF values are 1.330 and 1.287 s^{-1} for MnO_2/CeO_2-NR and Mn_2O_3/CeO_2-NR supported the better dispersion of Mn, as confirmed by the SEM-EDX (**Fig.5.6, and Fig. 5.7)** and XPS (**Fig. 5.3**, and **Fig. 5.4**). **Fig.5.12** illustrates the connection between surface lattice defects, surface oxygen, and reaction rates. Both graphs, **Fig.5.12(a)** and **Fig.5.12(b)** reveal that an increase in the catalyst's A_D/A_{F2g} and O_α leads to an increased reaction rate, consequently increasing NO conversion. This observed relationship is further validated by the NO conversion graph, highlighting the pivotal role of surface lattice defects and oxygen content in influencing the overall catalytic performance and emissions of nitrogen oxides (NO).

The Arrhenius plots of ln k versus reaction temperature were plotted in **Fig. 5.13(a)**. The activation energy of MnO_2/CeO_2-NR (75.14 KJ/mol) is lower than that of Mn_2O_3/CeO_2-NR (78.75 KJ/mol) and MnO/CeO_2-NR (85.17 KJ/mol), indicating that MnO_2/CeO_2-NR catalyst is the most effective for NO conversion.

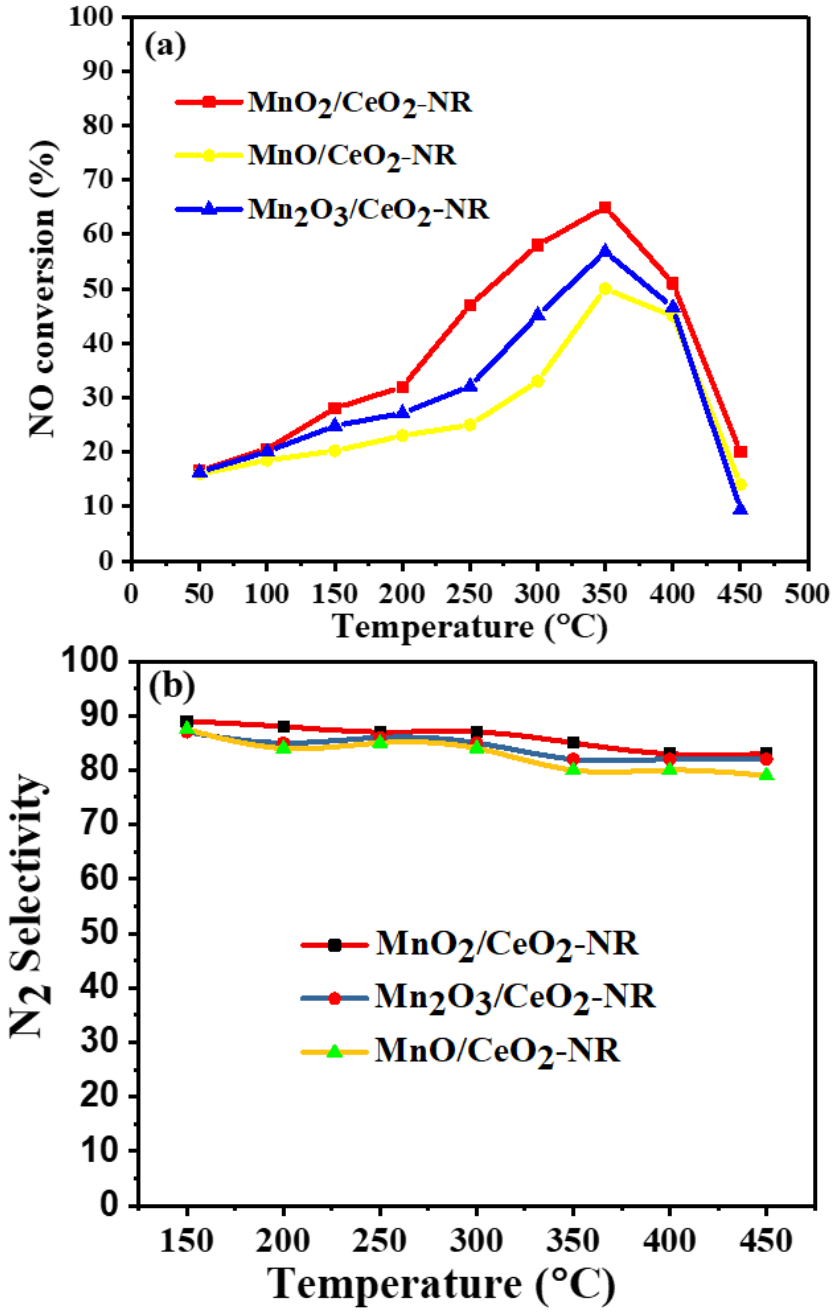

Fig. 5.11. Effects of temperature (a) NO conversions and (b) N_2 selectivity of the catalyst

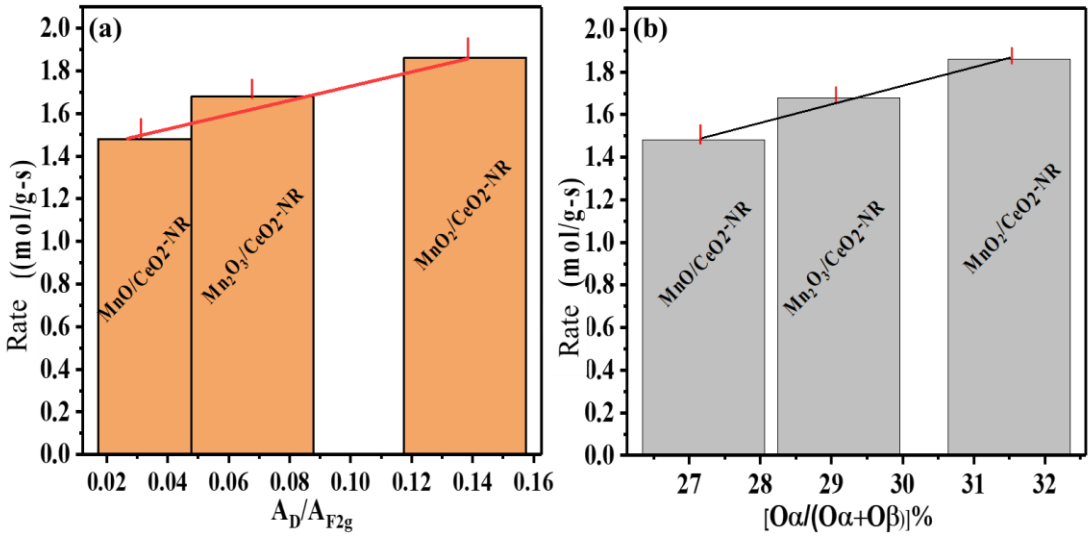

Fig. 5.12. Effect of (a) surface lattice defects and (b) surface oxygen on reaction rate

Table 5.6. Turnover frequency (TOF) of the samples at different temperatures

Catalyst	TOF (s^{-1}) at 250°C	TOF (s^{-1}) at 300°C	TOF (s^{-1}) at 350°C	TOF (s^{-1}) at 400°C
MnO/CeO_2-NR	0.702	0.768	1.195	1.066
Mn_2O_3/CeO_2-NR	0.981	1.027	1.287	1.059
MnO_2/CeO_2-NR	1.021	1.184	1.330	1.044

5.2.8.2. Stability of the catalysts with time

The practical-scale effectiveness of NH_3-SCR catalysts hinges on their long-term stability. The durability of MnO_2/CeO_2-NR catalyst was performed for 25 h at 350°C (**Fig. 5.13(b)**). No significant in NO conversion and N_2 selectivity was observed for the whole duration. Notably, the MnO_2/CeO_2-NR catalyst exhibited exceptional stability, with virtually no deactivation observed throughout the entire 25 h period. This underscores its reliability and suitability for sustained NO reduction applications in NH_3-SCR systems.

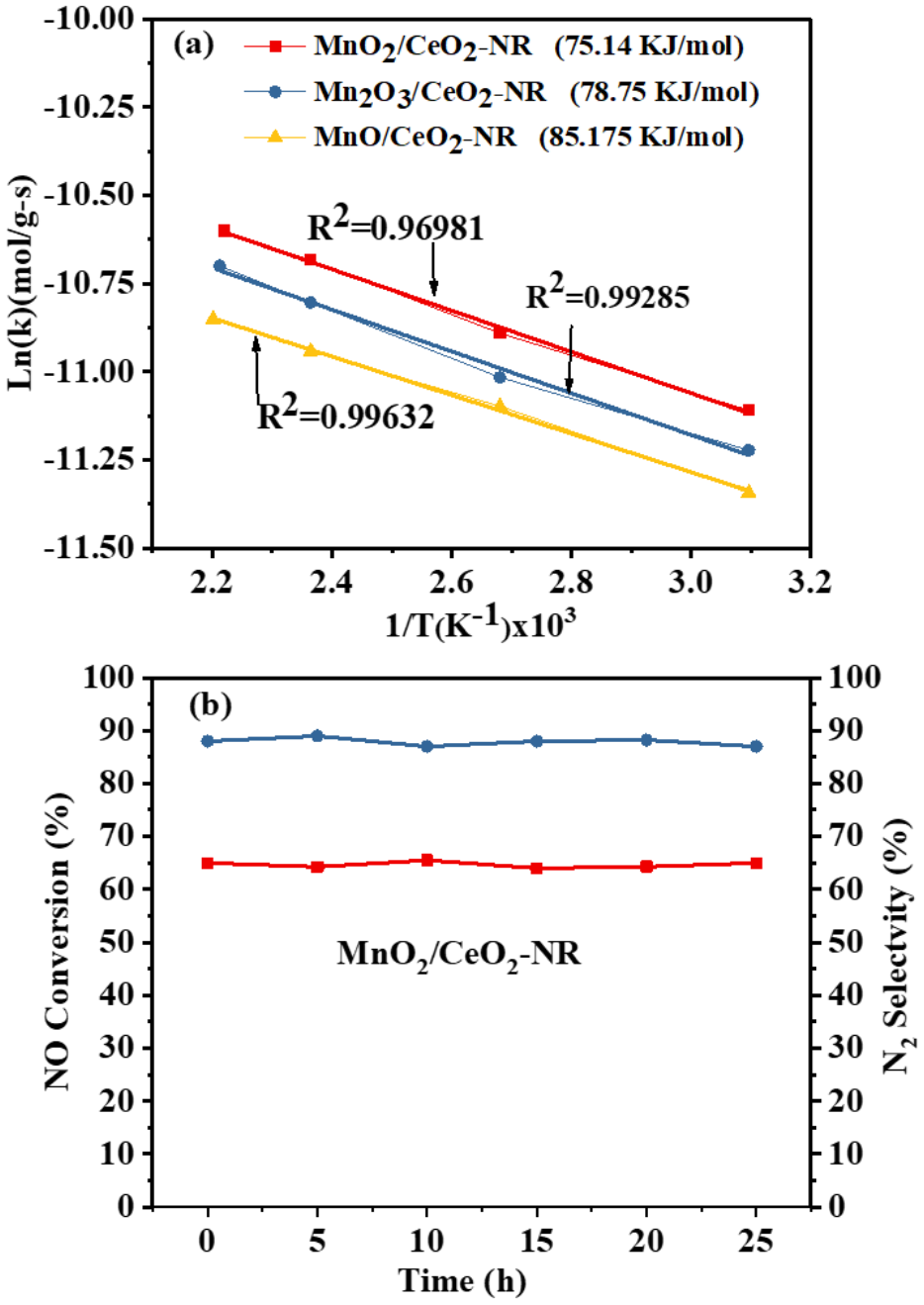

Fig. 5.13. (a) Arrhenius plot, and (b) Stability test of the catalyst

5.2.8.3. Effects of MnO_2 loading on catalyst for NO reduction

The effect of the amount of active metals on the catalyst was investigated for different mass ratios and the results are shown in **Fig. 5.14**. The reaction conditions which were optimized previously (MnO_2/CeO_2) were used to examined the catalytic activity. The NO conversion

profiles of MnO_2/CeO_2-NR catalyst (5 wt. %, 8 wt. %, 11 wt. %, 14 wt. %, 17 wt. %, and 20 wt.%) as a function of reaction temperature are shown in **Fig. 5.14(a)**. It can be noticed that adding MnO_2 to the CeO_2-NR supports increased the catalytic activity, and NO conversion was over 90% between the temperature 300–350°C with catalysts containing more than 14 wt.% MnO_2/CeO_2-NR. From the graph, it can be observed that the increased MnO_2 loading resulted in an increased NO conversion. Increasing the loading amount of MnO_2 also improves the N_2 selectivity as shown in **Fig. 5.14(b)**. But for 17 wt.% and 20 wt.%, maximum NO conversion is nearly the same at a temperature range between 200 to 350°C; it may be due to the blocking of active pore volume on impregnation of MnO_2 on supports above desired limit. Aside from unoptimized synergism between MnO_2 and CeO_2-NR, the significant agglomeration or cluster formation by MnO_2, as seen by a decrease in its surface area, could also be the reason for low NO conversion activity at higher loadings of 20 wt.%. However, when it comes to N_2 selectivity, the 20 wt.% MnO_2/CeO_2-NR has a greater N_2 selectivity than the total MnO_2 loading over CeO_2-NR. There is no conclusive data; however, it may be expected that N_2 selectivity is independent of catalyst surface area and pore volume and is most likely dependent on other physicochemical factors like Ce^{3+} and adsorbed oxygen.

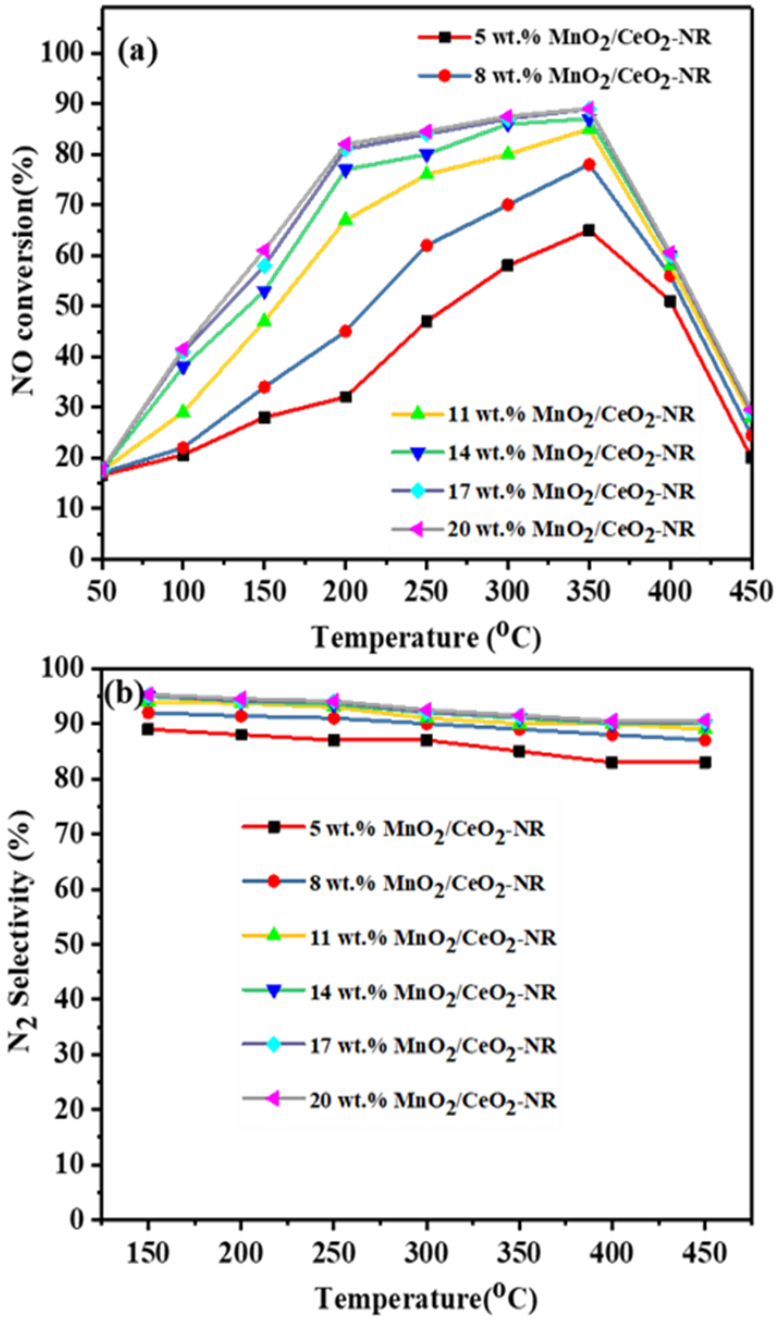

Fig.5.14. Effects of MnO_2 loading (a) NO conversions and (b) N_2 selectivity

5.2.8.4. Characterization of spent catalysts

Fig.5.15 shows the XRD pattern of all spent catalysts. There was no significant deviation on the diffraction pattern in comparison to **Fig.5.2**, but peak sharpness increased. **Table 5.7** shows

an increase in catalyst crystal size, which may be caused by cluster formation at high temperatures.

Fig.5.16 shows TEM images of the spent catalysts. The catalysts exhibited the same morphology, which suggests that the effects of high temperature did not affect their morphology properties. However, some catalysts exhibited larger particles, which may be caused by clustering.

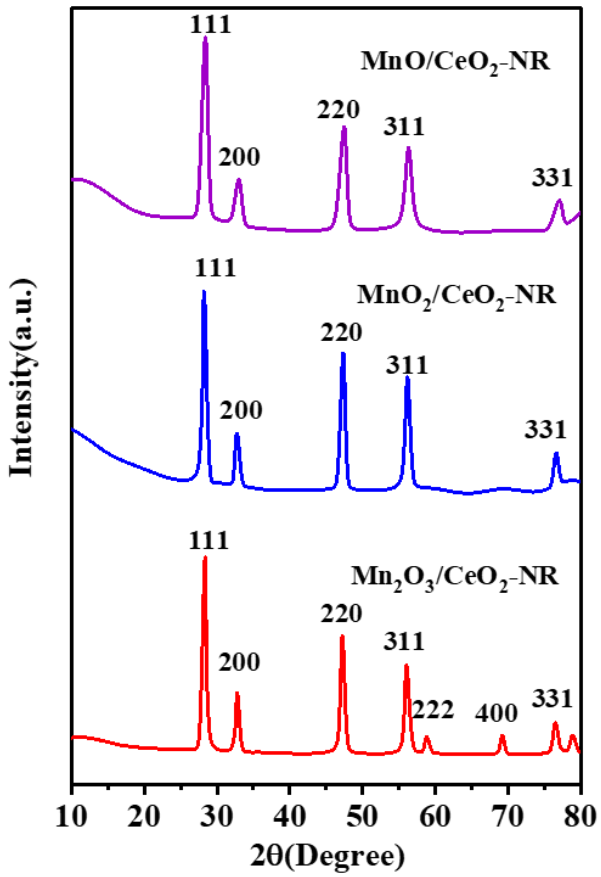

Fig. 5.15. XRD of spent MnO/CeO_2-NR, MnO_2/CeO_2-NR, and Mn_2O_3/CeO_2-NR catalysts

Table 5.7. Average crystal size and particle size of the spent catalysts

Catalyst	Average crystal size (nm)	Average particle size (nm)
MnO/CeO_2-NP	14.21	65
MnO_2/CeO_2-NC	13.27	84
Mn_2O_3/CeO_2-NR	15.33	92

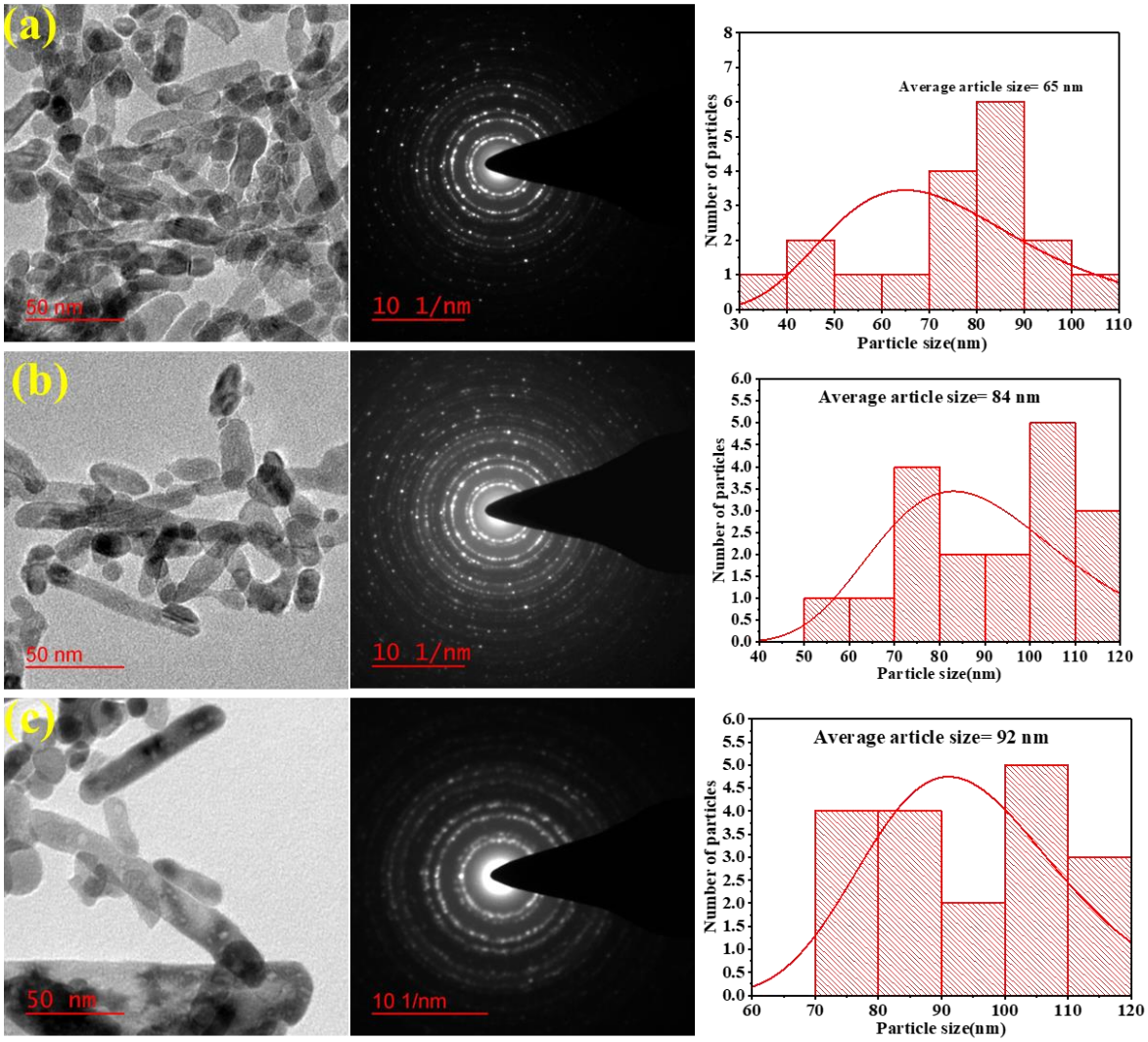

Fig. 5.16. TEM images of (a) spent MnO_2/CeO_2-NR, (b) spent Mn_2O_3/CeO_2-NR, and (c) spent MnO/CeO_2-NR catalysts

5.3. Conclusions

In conclusion, the hydrothermal followed the wet-impregnation approach successfully synthesized MnO_x/CeO_2-NR catalysts. The MnO_x dispersion significantly affected the performance of the obtained catalyst. The NO conversion (65%) and N_2 selectivity (89%) for the MnO_2/CeO_2-NR catalyst was highest in the wide temperature window range of 50-450℃. The outstanding performance of MnO_2/CeO_2-NR catalysts is due to the following reasons; high specific surface area and pore volume, well and homogenous distribution of active metals on supports, and more oxygen vacancies on MnO_2/CeO_2-NR, Mn^{4+} species, and Ce^{3+} species than the other two catalysts. More oxygen vacancies can promote oxygen absorption and active surface oxygen formation; Mn^{4+} concentration could speed up the SCR reaction by stimulating the conversion of NO to NO_2.

References

1. Damma, D., Ettireddy, P.R., Reddy, B.M. and Smirniotis, P.G., 2019. A review of low temperature NH3-SCR for removal of NO_x. *Catalysts*, *9*(4), p.349.
2. Li, J., Chang, H., Ma, L., Hao, J. and Yang, R.T., 2011. Low-temperature selective catalytic reduction of NO_x with NH_3 over metal oxide and zeolite catalysts-A review. *Catalysis today*, *175*(1), pp.147-156.
3. Zhai, G., Han, Z., Wu, X., Du, H., Gao, Y., Yang, S., Song, L., Dong, J. and Pan, X., 2021. Pr-modified MnO_x catalysts for selective reduction of NO with NH_3 at low temperature. Journal of the Taiwan Institute of Chemical Engineers, 125, pp.132-140.
4. Huang, F., Ye, D., Guo, X., Zhan, W., Guo, Y., Wang, L., Wang, Y. and Guo, Y., 2020. Effect of ceria morphology on the performance of MnO_x/CeO_2 catalysts in catalytic combustion of N, N-dimethylformamide. Catalysis Science & Technology, 10(8), pp.2473-2483.
5. Sunder Rao, S., Kumar Patel, V. and Sharma, S., 2022. Selective Catalytic Reduction of NO_x with NH_3 over Mn_2O_3 supported with different morphology of CeO_2 Catalysts. ChemistrySelect, 7(29), p.e202200302.
6. Chen, L., Wu, D., Wang, C., Ji, M. and Wu, Z., 2021. Study on Cu-Fe/CeO_2 bimetallic catalyst for reverse water gas shift reaction. Journal of Environmental Chemical Engineering, 9(3), p.105183.
7. Yun, J., Wu, L., Hao, Q., Teng, Z., Gao, X., Dou, B. and Bin, F., 2022. Non-equilibrium plasma enhanced oxygen vacancies of CuO/CeO_2 nanorod catalysts for toluene oxidation. Journal of Environmental Chemical Engineering, 10(3), p.107847.
8. Patel, V.K. and Sharma, S., 2021. Effect of oxide supports on palladium-based catalysts for NO reduction by H_2-SCR. Catalysis Today, 375, pp.591-600.

9. Liao, S., Qin, X., Luo, L., Han, Y., Wang, X., Usman, B., Nawaz, G., Zhao, N., Liu, Y. and Li, R., 2019. CRISPR/Cas9-induced mutagenesis of semi-rolled leaf1, 2 confers curled leaf phenotype and drought tolerance by influencing protein expression patterns and ROS scavenging in rice (Oryza sativa L.). Agronomy, 9(11), p.728.
10. Li, W., Zhang, C., Li, X., Tan, P., Zhou, A., Fang, Q. and Chen, G., 2018. Ho-modified Mn-Ce/TiO_2 for low-temperature SCR of NO_x with NH_3: Evaluation and characterization. Chinese Journal of Catalysis, 39(10), pp.1653-1663.
11. Huang, Y.Y., Zhao, T.S., Zhao, G., Yan, X.H. and Xu, K., 2016. Manganese-tuned chemical etching of a platinum–copper nanocatalyst with platinum-rich surfaces. Journal of Power Sources, 304, pp.74-80.
12. Kunchala, R.K., Pushpendra, Kalia, R. and Naidu, B.S., 2021. Irregularly shaped Mn_2O_3 nanostructures with high surface area for water oxidation. ACS Applied Nano Materials, 4(1), pp.396-405.
13. Rahman, M.M., Alam, M.M. and Asiri, A.M., 2019. Detection of toxic choline based on Mn_2O_3/NiO nanomaterials by an electrochemical method. RSC advances, 9(60), pp.35146-35157.
14. Xie, G., Liu, X., Li, Q., Lin, H., Li, Y., Nie, M. and Qin, L., 2017. The evolution of α-MnO_2 from hollow cubes to hollow spheres and their electrochemical performance for supercapacitors. Journal of Materials Science, 52, pp.10915-10926.
15. Zhao, X., Liu, X., Li, F. and Huang, M., 2020. MnO_2@ NiO nanosheets@ nanowires hierarchical structures with enhanced super capacitive properties. Journal of Materials Science, 55(6), pp.2482-2491.
16. Li, M., Lei, W., Yu, Y., Yang, W., Li, J., Chen, D., Xu, S., Feng, M. and Li, H., 2018. High-performance asymmetric supercapacitors based on monodisperse MnO nanocrystals with high energy densities. Nanoscale, 10(34), pp.15926-15931.

17. Yang, M., Shen, G., Wang, Q., Deng, K., Liu, M., Chen, Y., Gong, Y. and Wang, Z., 2021. Roles of oxygen vacancies of CeO_2 and Mn-doped CeO_2 with the same morphology in benzene catalytic oxidation. Molecules, 26(21), p.6363.
18. Wang, Q., Wang, R., Huang, X. and Shi, H., 2022. Sulfur/water resistance and regeneration of MnO_x-CeO_2/TiO_2 catalyst for low-temperature selective catalytic reduction of NO_x. Journal of Environmental Chemical Engineering, 10(2), p.107345.
19. Mingshan, C.U.I., Yuan, L.I., Xinquan, W.A.N.G., Jun, W.A.N.G. and Meiqing, S.H.E.N., 2013. Effect of preparation method on MnO_x-CeO_2 catalysts for NO oxidation. Journal of Rare Earths, 31(6), pp.572-576.
20. Wang, H., Wang, L., Luo, Q., Zhang, J., Wang, C., Ge, X., Zhang, W., and Xiao, F.S., 2022. Two-dimensional manganese oxide on ceria for the catalytic partial oxidation of hydrocarbons. Chemical Synthesis, 2(1), p.2.
21. Zhu, J., Zhang, G., Xian, G., Zhang, N. and Li, J., 2019. A high-efficiency CuO/CeO_2 catalyst for diclofenac degradation in Fenton-like system. *Frontiers in chemistry*, *7*, p.796.
22. Lin, X., Li, S., He, H., Wu, Z., Wu, J., Chen, L., Ye, D. and Fu, M., 2018. Evolution of oxygen vacancies in MnO_x-CeO_2 mixed oxides for soot oxidation. *Applied Catalysis B: Environmental*, *223*, pp.91-102.